Review Article | Musculoskeletal Imaging

eISSN 2005-8330
https://doi.org/10.3348/kjr.2023.0150
Korean J Radiol 2023;24(11):1114-1130

Korean Journal of Radiology
KJR

An Updated Review of Magnetic Resonance Neurography for Plexus Imaging

Joon-Yong Jung[1], Yenpo Lin[2,3], John A Carrino[2]

[1]Department of Radiology, Seoul St. Mary's Hospital, College of Medicine, The Catholic University of Korea, Seoul, Republic of Korea
[2]Department of Radiology and Imaging, Hospital for Special Surgery, Weill Cornell Medicine, New York, NY, USA
[3]Department of Medical Imaging and Intervention, Chang Gung Memorial Hospital, Taoyuan, Taiwan

Magnetic resonance neurography (MRN) is increasingly used to visualize peripheral nerves in vivo. However, the implementation and interpretation of MRN in the brachial and lumbosacral plexi are challenging because of the anatomical complexity and technical limitations. The purpose of this article was to review the clinical context of MRN, describe advanced magnetic resonance (MR) techniques for plexus imaging, and list the general categories of utility of MRN with pertinent imaging examples. The selection and optimization of MR sequences are centered on the homogeneous suppression of fat and blood vessels while enhancing the visibility of the plexus and its branches. Standard 2D fast spin-echo sequences are essential to assess morphology and signal intensity of nerves. Moreover, nerve-selective 3D isotropic images allow improved visualization of nerves and multiplanar reconstruction along their course. Diffusion-weighted and diffusion-tensor images offer microscopic and functional insights into peripheral nerves. The interpretation of MRN in the brachial and lumbosacral plexi should be based on a thorough understanding of their anatomy and pathophysiology. Anatomical landmarks assist in identifying brachial and lumbosacral plexus components of interest. Thus, understanding the varying patterns of nerve abnormalities facilitates the interpretation of aberrant findings.

Keywords: MRI; Neurography; Brachial plexus; Lumbosacral plexus; Diffusion tensor

INTRODUCTION

Magnetic resonance neurography (MRN) is an magnetic resonance imaging (MRI) technique dedicated to visualize peripheral nerves. The basic concept of MRN is to permit nerves to distinguish themselves from the surrounding tissue by suppressing the surrounding fat, muscles, and vessels using a combination of specific suppression techniques [1,2]. However, limitations in signal-to-noise ratio (SNR) and spatial resolution prevent earlier clinical use. Therefore, more than a decade was required to establish MRN as a clinically usable technique. Specifically, the widespread use of 3T scanners has expedited technical maturation by introducing isotropic three-dimensional (3D) images and functional imaging, such as diffusion-weighted or diffusion-tensor imaging, as part of the MRN protocol. Currently, MRN is evolving toward optimization in morphological imaging and robustness in quantitative imaging.

The brachial and lumbosacral plexi are groups of nerve bundles that interconnect the spinal nerve roots and peripheral nerves of the upper and lower limbs. The diagnosis of neuropathy involving the brachial and lumbosacral plexi is based on neurological examinations, electrophysiological studies, and surgical exploration [3,4]. However, MRI allows the correlation of clinical findings with imaging by visualizing nerve morphology in vivo. Furthermore, MRN provides a clear view along the peripheral nerve and offers a quantitative assessment of the nerves. Information regarding MRN significantly impacts diagnostic thinking and therapeutic management [5].

Despite technical advancements, applying MRN to the brachial and lumbosacral plexi remains challenging because

Received: February 15, 2023 **Revised:** August 2, 2023
Accepted: August 6, 2023
Corresponding author: John A Carrino, MD, MPH, Department of Radiology and Imaging, Hospital for Special Surgery, Weill Cornell Medicine, 535 East 70th Street, New York 10021, NY, USA
• E-mail: CarrinoJ@hss.edu

Korean Journal of Radiology
KJR

of their anatomic complexity and technical requirements for high spatial resolution over a wide field of view (FOV). This article reviews basic and advanced MRI techniques for plexus imaging and discusses image-based anatomy and pathology of the plexus in the context of MRN.

Imaging Protocol

Consideration in Preparation for Pre-scan

3T MRI is generally preferable for MRN because of its inherent gain in SNR, which can be exploited to boost the temporal, spatial, or contrast resolution compared with 1.5T [6]. In MRN, where spatial resolution is prioritized to perceive the nerve's fine details, the SNR gain is focused on enhancing spatial resolution. Therefore, acceleration techniques commonly used in joint or spine imaging are not encouraged in MRN, resulting in a longer protocol than conventional musculoskeletal imaging. However, 1.5T can be advantageous when metallic hardware is present inside the FOV [7].

A high-resolution MRN of the plexus requires appropriate selection and arrangement of the coils (Fig. 1). Dedicated high-resolution multichannel phased array surface coils are required for signal enhancement over a broader FOV without compromising the SNR. Increased flexibility enables the coils to be fitted across anatomical contours without gaps. In addition, a combination of coils may be required to cover the entire region of interest or assess muscle denervation. Thus, combining spinal array coils and multi-channel body matrix coils in a wrap-around fashion is an ideal configuration for the lumbosacral plexus [8]. However, coil selection in the brachial plexus is challenging because

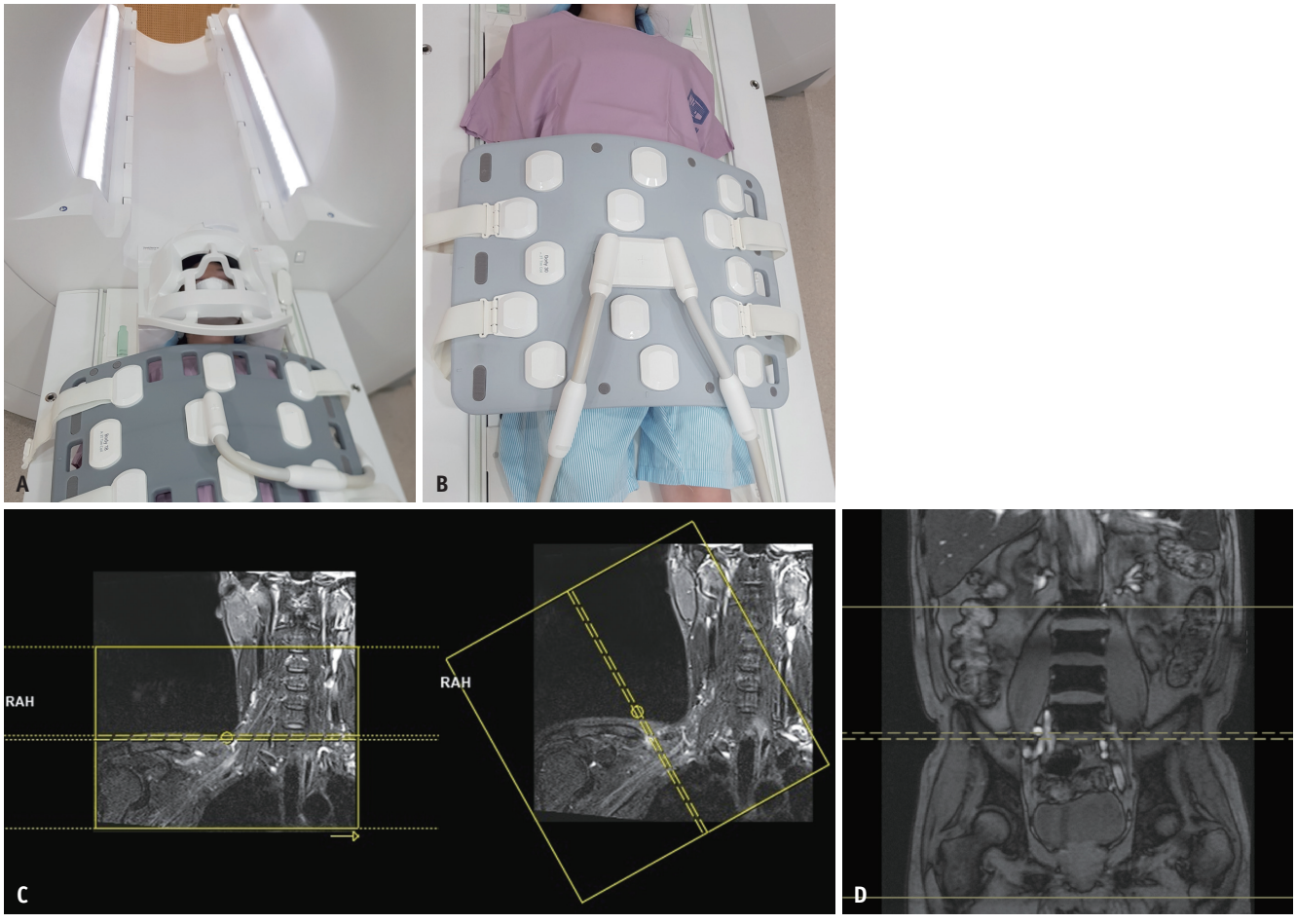

Fig. 1. Technique: coil placement and localization. **A:** Photograph showing how neurovascular array coil, spine array coil, and semi-flexible body matrix coil might be combined for brachial plexus imaging. **B:** Photograph showing how spine array coil and semi-flexible body matrix coil might be combined for lumbosacral plexus imaging. **C:** Brachial plexus localizer image prescriptions. An axial scan ranges from C4 down to the axilla level (left). An oblique sagittal plane was plotted on the coronal images, perpendicular to the brachial plexus (right). **D:** Lumbosacral plexus localizer image prescription. An axial scan ranges from L2 to the lesser trochanter of the femur. Yellow lines outline the boundaries of the scan range, and dashed yellow lines mean the center of the scan range.

https://doi.org/10.3348/kjr.2023.0150

of the curvature of the neck, shoulders, and axillary regions. In particular, a neurovascular array coil is placed along the anterior upper chest wall for bilateral imaging. To scan the unilateral brachial plexus, two semi-flexible coils positioned obliquely over and under the shoulder and neck are typically used [9]. The third option is to place two flexible coils around the shoulder and neck to concurrently obtain an appropriate SNR and coverage of both the supraclavicular and infraclavicular regions [10].

Respiratory movement degrades the infraclavicular segment of the brachial plexus on sagittal or oblique sagittal images orthogonal to the nerve course. However, prospective respiratory triggering effectively mitigates respiration-related motion artifacts and improves nerve conspicuity with a small time penalty [11] (Fig. 2).

Fat-suppression Techniques

Homogeneous fat suppression is essential for the MRN to improve nerve visibility. Frequency-selective fat suppression, widely used in musculoskeletal imaging, frequently fails because of field inhomogeneity caused by the complex geometry and large FOV. In contrast, short tau inversion recovery (STIR) is the most robust method for uniform fat suppression in any type of scanner; however, it suffers from poor SNR, pulsation artifacts, and a tendency to increase nerve signals [8]. T2-weighted spectral adiabatic inversion recovery (SPAIR) is a good alternative to STIR because it provides fat suppression similar to STIR, with a high SNR and fewer pulsation artifacts. The Dixon method is also useful for homogeneous fat suppression without an SNR penalty in the MRN. Dixon-based fat suppression exploits the difference in precession frequencies between fat and water and provides homogeneous fat suppression with an improved SNR compared to STIR. Once it was applicable with gradient-echo (GRE) images, it is now also suitable for fast spin-echo (FSE) sequences. However, it fails to provide uniform fat suppression near the metal, and an undesirable fat-to-water swap occurs [12].

The water excitation (WE) technique uses two excitation pulses with an intervening time lag to excite water preferentially using a second pulse. Owing to its high SNR and insensitivity to B1 inhomogeneity, it is commonly used

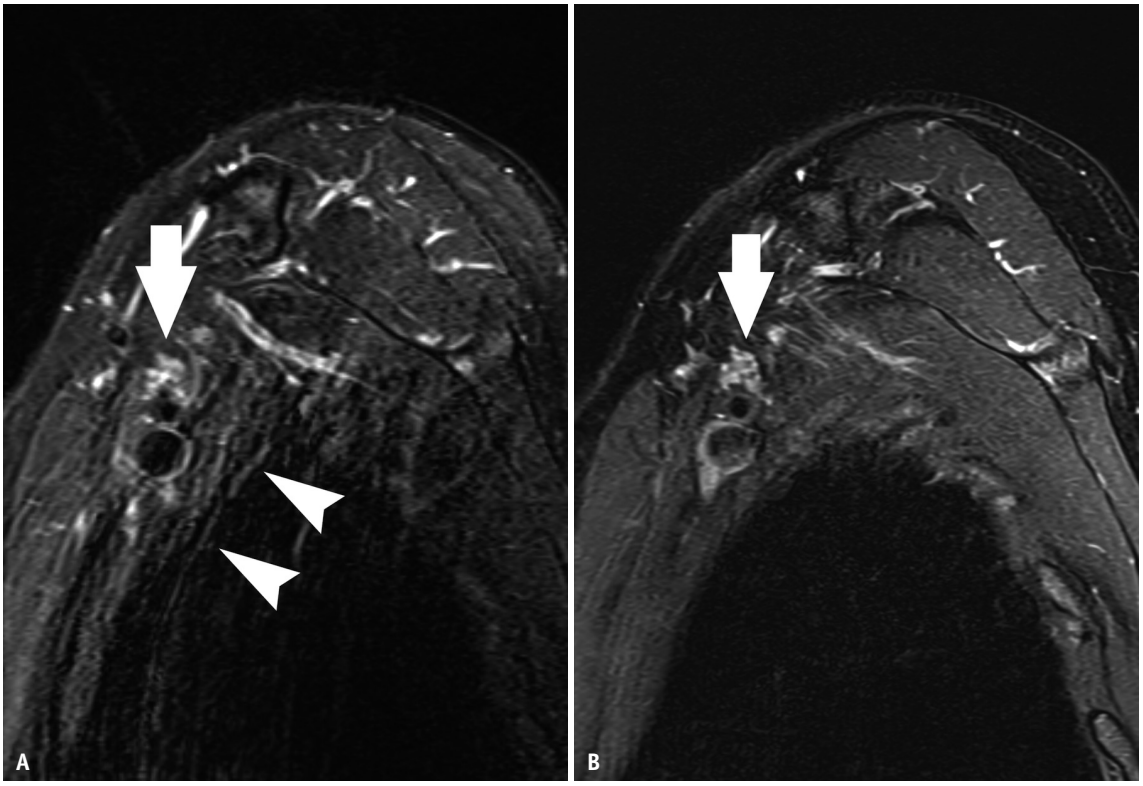

Fig. 2. Technique: respiratory triggering. Oblique sagittal chemical shift-encoded water-fat (Dixon method) water images with and without respiratory triggering. **A:** Without respiratory triggering, the brachial plexus (arrow) is blurred due to respiratory motion artifacts (arrowheads). **B:** With respiratory triggering, the respiratory motion artifact is suppressed; consequently, individual bundles (arrow) are more conspicuous. The scan time increased by approximately 15%–20%.

https://doi.org/10.3348/kjr.2023.0150

Korean Journal of Radiology
KJR

with GRE sequences. Despite its extensive use in scanners with low field strengths for fat suppression, the WE is also advantageous for 3T scanners because of the wider spectral separation between water and fat and shorter inter-excitation period [12].

Conventional Sequences

Fascicular abnormalities are more conspicuous in high-resolution images. Therefore, the MRN protocol includes high-resolution two-dimensional (2D) sequences with a matrix size greater than 256 in both directions. 2D sequences are obtained in the planes longitudinal and orthogonal to the plexus course. Furthermore, the coronal plane shows the entire course of the plexus and its branches, whereas the orthogonal planes (sagittal for the brachial plexus and axial for the lumbosacral plexus) depict the cross-sectional architecture of the nerve. Compared with true sagittal images, oblique sagittal 2D images facilitate the assessment of fascicular structures in the brachial plexus [13]. Although high-resolution 2D T2-weighted images orthogonal to the nerve course are often sufficient to detect and characterize nerve lesions, T1-weighted images acquired in the same plane delineate nerve anatomy and perineural fat planes. Notably, proton-density-weighted images without fat suppression can replace T1-weighted images because of their superior contrast resolution compared to adjacent muscles [10], and fluid-sensitive 2D sequences are essential for assessing signal changes, swelling, and the fascicular architecture of nerves. Lastly, 2D sequences also play a significant role in depicting muscle denervation changes (Fig. 3).

Isotropic 3D imaging is a fundamental component of the MRN protocol because it enhances peripheral nerve delineation by minimizing the partial volume averaging effect and permits multiplanar reformation along the longitudinal axis of nerves [14]. In particular, a 3D FSE with a smaller flip angle overcomes the specific absorption rate problem related to an increased echo train length and simulates the tissue contrast of a 2D FSE by designing refocusing pulses with varying flip angles. These sequences are commonly paired with fat suppression techniques to enhance nerve visibility. However, signals from peripheral veins with sluggish blood flow impede nerve identification. Therefore, 3D nerve-selective sequences that utilize blood signal suppression strategies are preferred.

Nerve-selective Sequences

3D diffusion-weighted reversed imaging with steady-state precession (DW-PSIF) is a steady-state free-precession sequence that collects only spin-echo-like signal components via time reversal [15]. Interestingly, the echo time (TE) in this sequence is longer than the repetition time (TR) because the radiofrequency (RF) pulse generates a spin-echo by refocusing the excitation signal in the previous RF pulse. Moreover, prolonged TE in DW-PSIF leads to heavy T2-weighted contrast and further dephasing of the transverse magnetization of moving protons [16]. In addition, a low-grade diffusion gradient was combined to

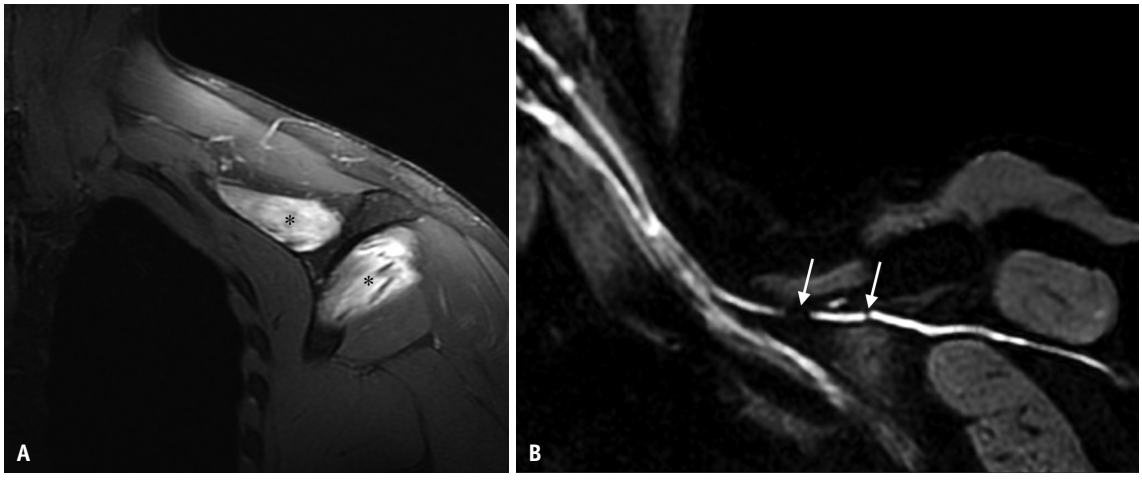

Fig. 3. Pathology: Parsonage-Turner syndrome. A 36-year-old male with motor weakness due to hourglass constrictions. **A:** Coronal 2D chemical-shift-encoded water-fat (Dixon method) water image demonstrates denervation edema involving the supraspinatus and infraspinatus muscles (asterisks), which are innervated by the suprascapular nerve. **B:** Coronal maximal intensity projection image of post-contrast 3D T2-weighted short tau inversion recovery fast spin-echo (STIR-FSE) depicts the hourglass constrictions involving suprascapular nerve (arrows). 2D = two-dimensional, 3D = three-dimensional

https://doi.org/10.3348/kjr.2023.0150

accentuate the dephasing of the vascular signal. Notably, WE technique permits homogeneous fat suppression without chemical-shift effects. However, this sequence is susceptible to local field inhomogeneity and poor SNR. Therefore, this technique is now recommended for MRN of the extremities, where the FOV is relatively small compared with plexus imaging. In addition, vascular flow suppression is incomplete because the vascular signal fluctuates depending on the orientation of the vessels with respect to the imaging plane [17].

A dual-echo steady-state sequence (DESS) or multi-echo in steady-state acquisition (MENSA) is a 3D GRE steady-state sequence that captures free induction decay in a steady-state precession sequence and the spin-echo in the PSIF sequence separately in one TR and combines the two images to form a single image [16]. DESS was originally favored for cartilage imaging but was recently expanded to MRN [18]. The first image provides a clear anatomical demarcation that is primarily defined by T1/T2*, whereas the second image with a heavily T2-weighted contrast adds a high signal to the peripheral nerves. The innate saturation effect and propensity to dephase in steady-state GRE contribute to the suppression of blood vessels.

The 3D nerve sheath signal increased with inked rest-tissue rapid acquisition of relaxation imaging (SHINKEI) is a 3D FSE sequence combined with an adiabatic inversion recovery pulse for robust fat suppression and an improved motion-sensitized driven-equilibrium pulse (iMSDE) for vascular suppression and signal amplification of peripheral nerves [19,20]. Motion-sensitized-driven-equilibrium (MSDE) uses motion-sensitizing diffusion gradients to suppress vascular flow and driven-equilibrium pulse to amplify the nerve signal by reversing residual transverse magnetization to longitudinal plane [21]. Improved MSDE (iMSDE) employs additional refocusing pulses and gradients to reduce eddy current and local B1 field inhomogeneity, thereby achieving a higher SNR [22]. Therefore, this technique is particularly advantageous when evaluating the brachial and lumbar plexi, where fat and vascular suppression are more difficult to achieve. SHINKEI demonstrated superior SNR and contrast-to-noise ratio for plexus imaging with efficient vascular suppression compared to 3D FSE STIR [10,20] and enabled nerve-selective imaging with increased conspicuity of the smaller lumbosacral plexus branches (Fig. 4). Tables 1 and 2 show examples of the protocols for the brachial and lumbosacral plexi, respectively.

Vascular Suppression Using Contrast Media

Despite the use of vascular suppression techniques, vascular contamination persists in smaller vessels where the vascular flow is stagnant. Recently, gadolinium-enhanced STIR was proposed for robust vascular suppression, showing the efficient nullification of the signal intensity of gadolinium-enhanced tissue, which has an inversion time similar to fat [23]. Moreover, the gadolinium-enhanced 3D FSE STIR sequence demonstrated the brachial and lumbosacral plexi more clearly without venous contamination [24,25] (Fig. 5). Gadolinium-based

Fig. 4. Technique: nerve-selective three-dimensional (3D) sequences of lumbosacral plexus. **A:** Coronal 3D T2-weighted short tau inversion recovery fast spin-echo (STIR-FSE) with improved motion-sensitized driven-equilibrium (iMSDE). **B:** Coronal diffusion-weighted reversed imaging with steady-state precession (DW-PSIF). **C:** Coronal 3D dual-echo steady-state sequence (DESS). **D:** Coronal 3D nerve-sheath signal increased with inked rest-tissue rapid acquisition of relaxation imaging (SHINKEI) is a fast spin-echo with spectral attenuated inversion recovery (SPAIR) for fat suppression and iMSDE for vascular suppression and signal amplification of peripheral nerves.

https://doi.org/10.3348/kjr.2023.0150

Korean Journal of Radiology
KJR

Table 1. Unilateral brachial plexus protocol

Sequences	2D PDw FSE	2D T2w FSE	2D T1w FSE	2D T2w FSE	3D STIR FSE*
Imaging plane	Axial	Coronal	Oblique sagittal	Oblique sagittal	Oblique coronal
Fat suppression	-	Dixon	-	SPAIR	STIR
Vascular suppression	-	-	-	-	iMSDE
Field of view, cm	23	18	16	16	18
Matrix size	512 x 352	320 x 224	320 x 224	320 x 224	256 x 256
Slice thickness/interslice gap, mm	3.5/0	2.5/0	2.5/0	2.5/0	1/0
TR/TE, ms	4155/37	4300/85	690/11	4300/85	3300/60
Bandwidth, kHz	± 83.3	± 62.5	± 66.6	± 62.5	± 50
Echo-train length	15	14	3	14	130
Acceleration	1.5	1	1	1	1.1 x 1 x 1.1†
Scan time	2:00	4:00	3:20	4:00	6:30
Postprocessing	-	-	-	-	MPR (oblique sagittal), MIP with thin slab (10 mm)

*Alternatively, could be performed as a post-gadolinium acquisition without iMSDE, †Phase x slice x compressed sensing.
2D = two-dimensional, PDw = proton-density weighted, FSE = fast spin-echo, T2w = T2-weighted, T1w = T1-weighted, 3D = three-dimensional, STIR = short tau inversion recovery, SPAIR = spectral adiabatic inversion recovery, iMSDE = improved motion-sensitized driven-equilibrium, TR = repetition time, TE = echo time, MPR = multiplanar reformation, MIP = maximum-intensity projection

Table 2. Lumbosacral plexus protocol

Sequences	2D T1w FSE	2D T2w FSE	DTI	2D T1w FSE*	3D STIR FSE*
Imaging plane	Axial	Axial	Axial	Axial	Coronal
Fat suppression	-	SPAIR	SPAIR	Dixon	STIR
Vascular suppression	-	-	-	-	iMSDE
Field of view, cm	32	32	33	32	28
Matrix size	512 x 256	512 x 256	128 x 128	512 x 256	256 x 256
Slice thickness/interslice gap	5/0	5/0	5/0	5/0	1/0
TR/TE, ms	866/9.8	3500/68	6300/59	555/9.7	3000/250
Bandwidth, Hz/Pixel	241	888	2170	888	349
Echo-train length	3	14	88	3	120
Diffusion parameters	-	-	b = 0 and 800 s/mm^2, 6 direction	-	-
Acceleration/number of excitation	3/2	3/2	2	3/2	2 x 2 x 1†/1.4
Scan time	4:40	3:25	5:28	3:05	4:55
Postprocessing			MD and FA map		MPR (Sagittal and axial), MIP with thin slap (10 mm)

*Alternatively, could be performed as a post-gadolinium acquisition without iMSDE, †Phase x slice x compressed sensing.
2D = two-dimensional, T1w = T1-weighted, FSE = fast spin-echo, T2w = T2-weighted, DTI = diffusion-tensor imaging, 3D = three-dimensional, STIR = short tau inversion recovery, SPAIR = spectral adiabatic inversion recovery, iMSDE = improved motion-sensitized driven-equilibrium, TR = repetition time, TE = echo time, MD = mean diffusivity, FA = fractional anisotrophy, MPR = multiplanar reformation, MIP = maximum-intensity projection

vascular suppression can be combined with non-contrast vascular suppression techniques [10] or used separately. Comparatively, post-contrast STIR tends to outperform the MSDE and iMSDE techniques for vascular suppression.

Superparamagnetic iron-oxide nanoparticles have also been investigated as agents that suppress vascular signals. Ferumoxytol (Feraheme; AMAG Pharmaceuticals) was initially approved by the U.S. Food and Drug Administration for treating iron-deficiency anemia [26]; specifically, its greater effect on shortening the T2* relaxation time enables vascular suppression in fluid-sensitive sequences with a higher SNR than that in STIR. In addition, the imaging time is more flexible because it is a long-lasting blood-pool agent. A recent study reported improved qualitative and quantitative assessments of the brachial plexus using 3D STIR sequences after ferumoxytol injection [27]. However,

 https://doi.org/10.3348/kjr.2023.0150

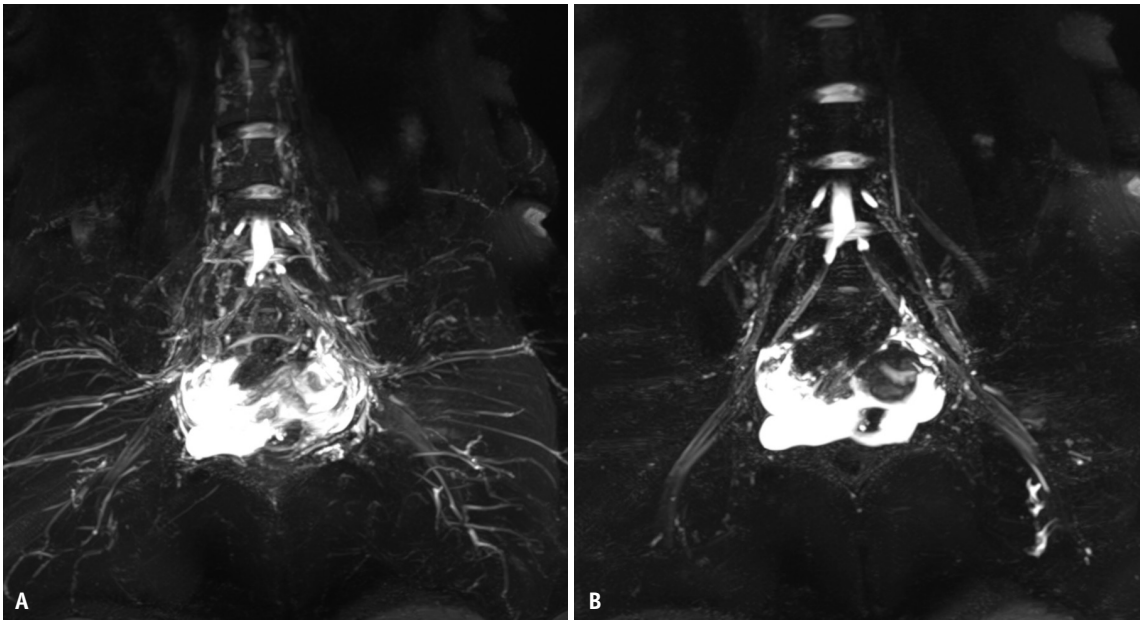

Fig. 5. Technique: effect of gadolinium contrast enhancement for vascular suppression. Coronal three-dimensional (3D) T2-weighted short tau inversion recovery fast spin-echo (STIR-FSE) maximal intensity projection images of the lumbosacral plexus. Before (pre-contrast STIR) **(A)** and after (post-contrast STIR) **(B)** administration of gadolinium intravenous contrast. Vascular signal suppression significantly improved following contrast administration. Post-contrast STIR improved the nerve-to-muscle contrast ratio, allowing for enhanced visualization and diagnostic confidence in the evaluation of branch nerves.

potential disadvantages of ferumoxytol include contrast retention in the liver and reduced workflow due to its slow infusion rate [10].

MRN with Metallic Instruments

Optimized pulse sequences enable MRN to examine the brachial and lumbosacral plexi adjacent to metallic devices. Although 1.5T is often preferred in the presence of metal, 3T is preferred for plexus evaluation in the context of shoulder or hip arthroplasty to acquire high-resolution images with sufficient SNR [28]. To perform MRN near metallic instruments, the type of metal and proximity of the imaged tissue to the metallic hardware should be considered. Doubling the receiver bandwidth and shrinking the voxel size with an increased number of excitations diminishes the distortion. When severe artifacts are anticipated or the plexus is close to metallic implants, multispectral imaging techniques such as slice encoding for metal artifact correction (SEMAC) or multi-acquisition variable resonance image combination (MAVRIC) can also be considered [7]. However, an alternative diagnostic modality may be suggested if magnetic susceptibility effects are expected to impede nerve visibility despite adjustments to MRI techniques.

Diffusion-weighted and Diffusion-tensor Images

Diffusion-weighted imaging (DWI) is a technique used to quantify the random thermal motion of water molecules (i.e., Brownian motion). Similar to the brain and spinal cord, DWI accurately depicts peripheral nerves with a relatively long T2 relaxation time and impeded diffusion [29]. The background signal was effectively suppressed using STIR and a heavy diffusion-sensitizing gradient [30]. Moreover, free-breathing during image acquisition facilitates background suppression and improves the efficiency of obtaining thin-slice images for 3D reformation. Thus, whole-body DWI has become a viable method for visualizing demyelinating diseases or hereditary neuropathy affecting the entire body at a glance [31].

Diffusion-tensor imaging (DTI) is a technique that measures directional water diffusion in peripheral nerves by applying additional diffusion-sensitizing gradients in at least six directions. Directional movement can be expressed by a tensor and matrix with nine components, which is visualized as a diffusion ellipsoid [32]. The four main parameters derived from the three eigenvalues of the ellipsoid are obtained using DTI [33]. Specifically, fractional anisotropy (FA) represents the degree of anisotropic diffusion within the fiber tracts. Mean diffusivity, which is equivalent to the apparent diffusion coefficient on

https://doi.org/10.3348/kjr.2023.0150

Korean Journal of Radiology
KJR

DWI, is the average of the three diagonal elements in the tensor. Axial diffusivity, the largest eigenvalue, represents the motion of diffusion and is the least hindered, thus reflecting the degree of axonal conduction. Lastly, radial diffusivity (RD), the average of the other two eigenvalues, represents water movement along the short axis of the nerve, thus indicating myelin integrity.

Tractography is the 3D representation of fiber tracks based on the orientation of the dominant fiber tracts in DTI. It is constructed using the eigenvector, orientation of the vector (eigenvector), and FA (eigenvalue). However, the fiber tracts are mathematical constructions based on the presumed connectedness of voxels with similar diffusion properties and do not correspond to axons or muscle fibers.

Many pathological processes in nerves can be quantitatively assessed using DTI (Fig. 6) [34]. For the diagnosis of mild peripheral neuropathy, FA maps outperformed nerve conduction studies [35]. In particular, monitoring the degenerative and regenerative processes of peripheral nerves is also a promising area in which DTI is the most valued. During the degenerative phase, the FA decreases and RD increases. In contrast, the regenerative process causes a progressive increase in FA values and a decrease in RD, indicating the restoration of anisotropy via

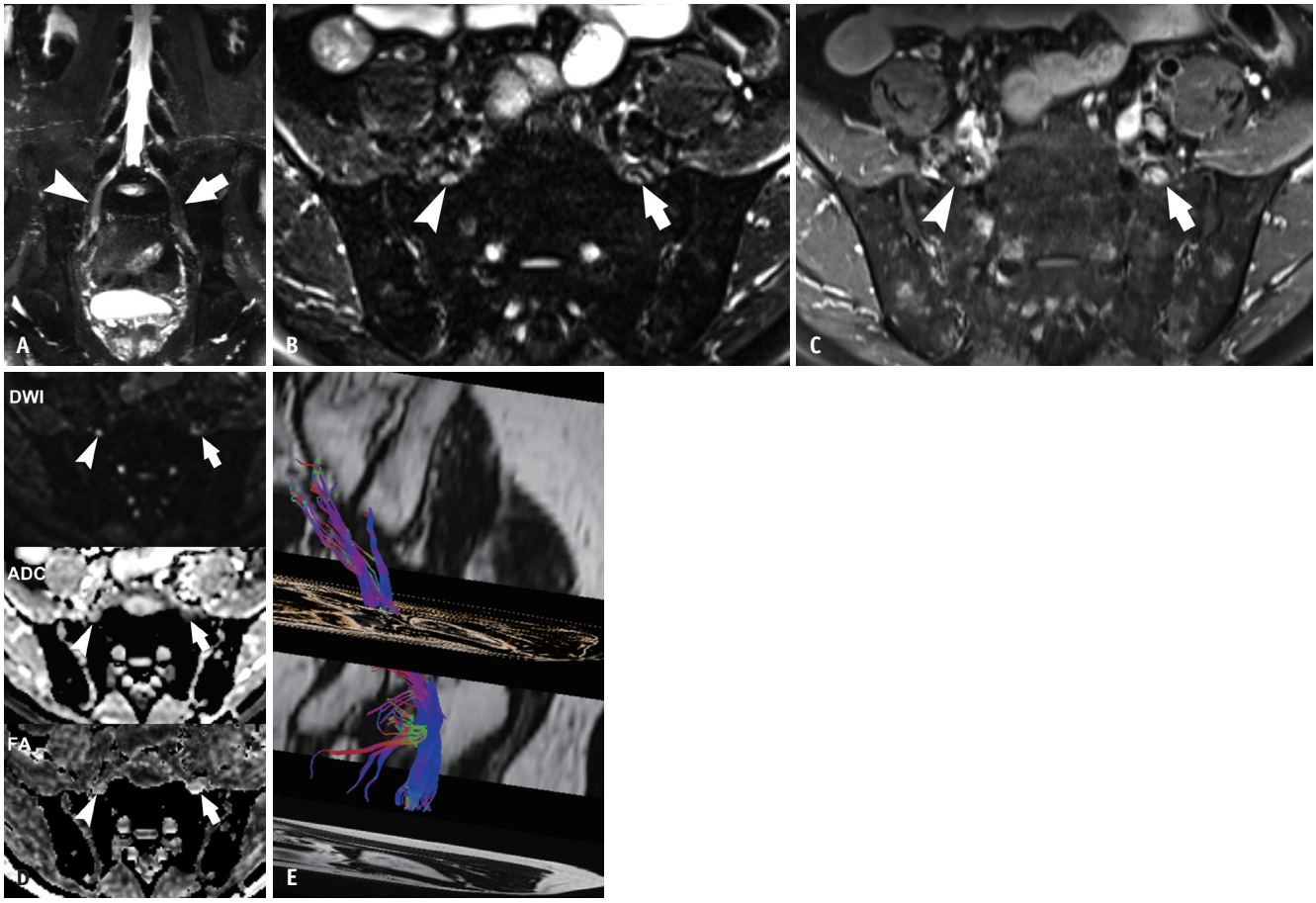

Fig. 6. Pathology: treatment effect. A 50-year-old male with left sciatica and motor leg weakness who had received chemotherapy for leukemia. **A:** Coronal three-dimensional (3D) T2-weighted short-tau inversion recovery fast spin-echo (STIR-FSE) with 10 mm-slab, maximal intensity projection demonstrates asymmetrical thickening of left S1 nerve (arrow) compared to right S1 (arrowhead). Axial fat-suppressed two-dimensional (2D) T2-weighted image **(B)** and gadolinium-enhanced fat-suppressed T1-weighted image **(C)** show enlargement and enhancement, respectively, of left S1 nerve (arrows), compared to right S1 nerve (arrowheads). **D:** Axial diffusion-weighted image (DWI) with a b-value of 600 and apparent diffusion coefficient (ADC) and fractional anisotropy (FA) maps, each at the same section selection, provide quantitative information on the peripheral nerves. The ADC measures 0.97 x 10^{-3} mm^2/s on the left S1 nerve (arrows) and 1.34 × 10^{-3} mm^2/s on the right S1 nerve (arrowheads). The FA measures 0.48 on the left S1 nerve (arrows) and 0.58 on the right S1 nerve (arrowheads). **E:** Tractography of the left lumbosacral plexus to the sciatic nerve shows no discontinuity along the nerve tract. The patient completely recovered symptomatically after radiation therapy for the left S1 lesion. This case illustrates how diffusion changes correlate to the clinical deficit and are potentially useful for early diagnosis and longitudinal evaluation, especially in pharmacological therapy.

https://doi.org/10.3348/kjr.2023.0150

nerve fiber reorganization [36]. Furthermore, tractography provides a 3D visualization of these processes [37].

However, DTI in the plexus imaging is technically more challenging than DTI in the brain. Despite the long acquisition time, the low SNRs of peripheral nerves and sampling of multiple diffusion directions compromise the image quality and precision of the quantitative parameters [38]. According to a recent study, the ideal b value for peripheral nerve DWI or DTI should be 700 sec/mm^2 or less in order to obtain a reliable value [39]. Another limitation is the intrinsic inhomogeneity of the local magnetic field, which leads to amplified image distortion and susceptibility artifact [40]. This can be mitigated by segmented echo-planar imaging or non-Cartesian sampling.

Image Improvement Using Artificial Intelligence

Given the requirement for high SNR and resolution in nerve evaluation, artificial intelligence-based image enhancement of MRN holds promise. Combining model-based and model-independent denoising techniques improves peripheral nerve conspicuity in DWI and FA map reproducibility [41]. Improving SNR and shortening the acquisition time were adversarial in traditional MR physics. However, deep-learning (DL)-based image enhancement can accomplish both. Specifically, DL-based image reconstruction improves image quality by increasing the SNR and edge sharpness while reducing the scan time. In 2D FSE, DL-reconstructed images significantly improve the visibility of the outer epineurium and fascicular architecture [42]. However, additional validations of DL-based reconstruction are required to address concerns regarding image fidelity [43].

Anatomy and Pathology of Peripheral Nerve and Plexus

Microanatomy of Peripheral Nerves

A neuron is composed of a cell body, an axon, and dendrites. The axon is a long, slender projection of a nerve that conducts electrical impulses. Myelin, developed by Schwann cells, surrounds the axons to enable fast conduction. In peripheral nerves, intricately organized connective tissue layers surround the nerve fibers for mechanical protection and functional support [44]. The connective tissue sheath around the nerve fibers is the endoneurium. Additionally, the fascicle, a bundle of nerve fibers, is surrounded by another connective tissue layer known as the perineurium. The fascicles are finally bundled together by a thick layer of connective tissue called the epineurium to form the peripheral nerves.

Larger nerves have more fascicles and thicker layers of connective tissue. In particular, each nerve fascicle consists of varying proportions of sensory, motor, and/or autonomic nerve fibers. The interfascicular epineurium also incorporates vessels and adipose tissue. Within the peripheral nerves, a vascular network comprising vessels coursing along the epineurium and perineurium extends into the endoneurial space. At the level of the perineurium and endoneurial capillaries, a blood-nerve barrier restricts plasma entry into the endoneurial space [45]. Functioning in a manner akin to a gliding layer, the outer and interfascicular epineurium facilitates motion of the fascicles. As a result, reorganization of fascicle configuration primarily occurs longitudinally along the nerve or in response to localized compression.

Pathology of Peripheral Nerves

Local lesions such as acute or chronic damage caused by trauma or entrapment, iatrogenic incidence, intrinsic or extrinsic neoplasms, and focal neural or perineural infection can affect the plexus. Systemic disorders affecting the plexus include chemotherapy- or radiation-induced plexopathy, metabolic diseases, amyloidosis, neurofibromatosis, and genetic diseases, such as Charcot Marie Tooth (CMT) disease. In compressive neuropathy, increased pressure causes hyperemia, axoplasmic flow blockage, venous congestion, and eventually proximal epineural edema, and distal Wallerian degeneration.

Nerve injury may involve axons, myelin, and the surrounding connective tissues in isolation or, more commonly, in combination. The regenerative potential of peripheral nerves depends on the integrity of the surrounding connective tissue. Therefore, injury grade is usually based on the extent of damage to the connective tissue layers of the nerve. Sprouting of the disrupted axons follows contact guidance when connective tissue layers are intact [46]. Notably, chemotactic factors released from distal targets also aid in directing sprouting axons to their correct destinations [47].

Seddon categorized three types of nerve damage according to severity [48]. First, neurapraxia is a local myelination injury that occurs without axonal damage. Nerve conduction study revealed a focal conduction block, which is fully restored within a few days to several weeks. Axonotmesis is

https://doi.org/10.3348/kjr.2023.0150

Korean Journal of Radiology
KJR

axonal loss without damage to the connective tissue layers. Second, Wallerian degeneration is triggered by axonotmesis to ensure the elimination and reformation of nerve fibers distal to the injury site. Third, neurotmesis is the most severe form, in which the nerve is completely severed. The recovery is only expected if the distal stump is surgically reconnected. Nerve conduction studies reveal that both axonotmesis and neurotmesis result in distal conduction loss at the lesion site [49].

Sunderland subdivided axonotmesis based on the differential involvement of three connective tissue layers, which is crucial for recovery potential [50]. In the Sunderland system, the second, third, and fourth grades represent axonal injury with varying degrees of injury to the endoneurial and perineurial tissues. The fifth grade, which is the complete discontinuity of nerve fibers and connective tissue layers, including the epineurium, is equivalent to neurotmesis. In the fourth and fifth grades, axonal regeneration usually fails to properly innervate the sensory endings or muscle endplates because the connective tissue sheaths are disrupted. Neuroma in continuity (NIC) is the characteristic morphology of a fourth-grade injury in which internal bleeding and fibrous tissue are entangled, inhibiting the formation of directed axons. Fifth-degree injury leads to the end-bulb neuroma and disorganized axon sprouting within the fibrotic matrix. Subsequently, the sixth grade, the most common type of direct nerve injury, was added [51]. The 6th-degree injury is one that involves multiple layers without following the conventional inside-outside pattern. Notably, the MRN can aid in classifying grades and identifying patients who would benefit from surgical intervention (Table 3) [52].

Imaging Anatomy of Brachial Plexus

The brachial plexus provides somatosensory and motor innervation to the chest wall and the entire upper extremity. Anatomical variations have been identified more frequently at the supraclavicular level than at the infraclavicular level. Five roots of brachial plexus originate from the ventral rami of the C5–T1 spinal nerves. Over the inferolateral course of the brachial plexus, the five roots converge to three trunks, diverge into six divisions, and again converge to three cords. The clavicle is a landmark in the superior to inferior direction, whereas the interscalene triangle, lateral border of 1st rib, and medial border of the coracoid process are landmarks in the mediolateral direction [53].

Table 3. Injury classifications for peripheral nerves

Seddon	Sunderland [50]*	Injury	MRI	Management and Prognosis
Neuropraxia	I	Myelin sheath	Muscle: normal Nerve: normal/mildly increased SI without swelling on T2wI	Conservative, full recovery
Axonotemesis	II	Axonal	Muscle: denervation Nerve: ↑ T2w SI & diffuse swelling Fascicles: enlarged or effaced	Conservative, full but prolonged recovery due to Wallerian degeneration
	III	Axonal + endoneurium	Muscle: denervation Nerve: ↑ T2w SI & diffuse swelling Fascicles: enlarged or effaced	Conservative, recovery with mild deficit due to hindered regeneration by mild fibrosis
	IV	Axonal + endoneurium + perineurium	Muscle: denervation Nerve: neuroma-in-continuity (heterogeneous localized swelling) Fascicles: disrupted	No recovery unless operational intervention
Neurotmesis	V	Complete nerve injury including epineurium	Muscle: denervation Nerve: complete transection of nerve with nerve gap or end bulb neuroma	No recovery unless operational intervention
	VI (Mackinnon and Dellon [51])	Mixed injury	Muscle: denervation Nerve: variable with perineural scarring (ill-defined soft tissue in perineural fat plane)	Variable, usually require operational intervention

*The classification is based on Sunderland [50], *Brain* 1951;74:491-516 and 'VI' is based on Mackinnon and Dellon [51], Thieme Medical Publishers, 1988.
MRI = magnetic resonance imaging, SI = signal intensity, T2wI = T2-weighted images, T2w = T2-weighted

 https://doi.org/10.3348/kjr.2023.0150

The upper trunk is formed by the union of the C5 and C6 roots, the middle trunk by the continuation of the C7 root, and the lower trunk by the union of the C8 and T1 roots. Occasionally, contributions from the C4 and T2 nerve roots can be observed, referred to as "prefixed" and "postfixed" plexus, respectively. The three trunks pass through the triangle created by the anterior and middle scalene muscles, and the posterior rib is the base of the triangle (supraclavicular). C5 and C6 roots can either pass anteriorly or through the anterior scalene muscle as a variant of anatomy [54]. At or near the lateral border of the first rib, each trunk bifurcates into anterior and posterior divisions, and above the subclavian artery and posterior to the mid-clavicle (retroclavicular), the three anterior and posterior divisions align to form a triangular cluster. At the division level, nerves are more functionally rearranged, with the anterior division innervating the flexor muscles and the posterior division innervating the extensor muscles [53]. At the level of the medial border of coracoid process (infraclavicular), the divisions unite to form the lateral, posterior, and medial cords. In the infraclavicular fossa, the cords encircle the axillary artery as follows: the lateral cord is anterior, the posterior cord is superior, and the medial cord is posterior to the artery. The cords finally divide into five terminal branches. The axillary nerve exits from the posterior cord as it winds underneath the scapular neck. The median, radial, ulnar, and musculocutaneous nerves are positioned around the axillary-brachial arteries distal to the superolateral border of the pectoralis minor. A visual representation of the aforementioned anatomical features is provided in Figure 7, which presents MRN images delineating each of these significant landmarks.

Multiple side branches arise from the brachial plexus during its course. The long thoracic nerve (C5-C7), dorsal scapular nerve (C5 root), and suprascapular nerve (upper trunk) originate in the supraclavicular plexus. However, the origins of these nerves are a significant source of anatomical variation.

Imaging Anatomy of Lumbosacral Plexus

The lumbosacral plexus innervates the lower trunk and lower extremities. The lumbar plexus is formed by the ventral rami of the L1 to L4 nerve roots, whereas the sacral plexus is produced by the ventral rami of the L4 to S3 nerve roots. The lumbosacral trunk, formed from the L5 and lesser branches of the L4 nerve roots, connects the two plexi and descends over the sacral ala and fuses with the S1 and S3 nerve roots in the anterior portion of the piriformis muscle to form the sacral plexus. In contrast to the brachial plexus, in which segments continue to intertwine before the terminal branches become longer, roots converge and promptly give forth the terminal branch or divisions that also merge shortly to produce the terminal branch. Consequently, terminal nerves constitute the majority of the lumbosacral plexus. The landmarks for locating nerve paths are essential for nerve identification. Figure 8 shows the MRN images of important terminal branches.

The lumbar plexus gives rise to the iliohypogastric, ilioinguinal, genitofemoral, obturator, and femoral nerves, and lateral femoral cutaneous nerve (LFCN). These nerves can be identified based on their exit from the psoas muscle. In particular, the iliohypogastric and ilioinguinal nerves (T12–L1) run along the lateral border of the psoas and quadratus lumborum muscles before passing through the lateral abdominal wall above the iliac crest. The genitofemoral nerve (L1–L2) runs anteriorly to the psoas muscle in a vertical path, with the medial genital branch entering the inguinal canal and the lateral femoral branch running lateral to the femoral artery.

The obturator nerve (the anterior divisions of L2, L3, and L4) descends vertically along the medial border of the psoas muscle and approaches the pelvic sidewall, and splits into anterior and posterior branches in the obturator foramen. The femoral nerve (posterior division of L2-L4) runs inferolaterally behind the psoas muscle, parallel to the LFCN, entering the femoral canal after vertically turning on the groove of the pelvic muscles. Lastly, the LFCN (L2–L3) runs anterolaterally through the iliacus muscle under the inguinal ligament medial to the anterior superior iliac spine.

The sacral plexus gives rise to the sciatic, pudendal, superior, and inferior gluteal nerves. The sciatic nerve is composed of the tibial nerve (anterior division of the lumbosacral trunk-S3) and the peroneal nerve (posterior division of the lumbosacral trunk-S2) in a shared nerve sheath. The nerve signal exhibits symmetrical augmentation owing to the magic angle artifact at the sciatic notch; however, this elevation returns to baseline levels posterior to the acetabular column. The classification system proposed by Beaton and Anson [55] delineates six distinct configurations characterizing the anatomical interrelationship between the sciatic nerve and the piriformis muscle, with original distributions identified parenthetically. Specifically, type A pertains to an uninterrupted nerve situated beneath the undivided muscle (84.2%). In

https://doi.org/10.3348/kjr.2023.0150

Korean Journal of Radiology
KJR

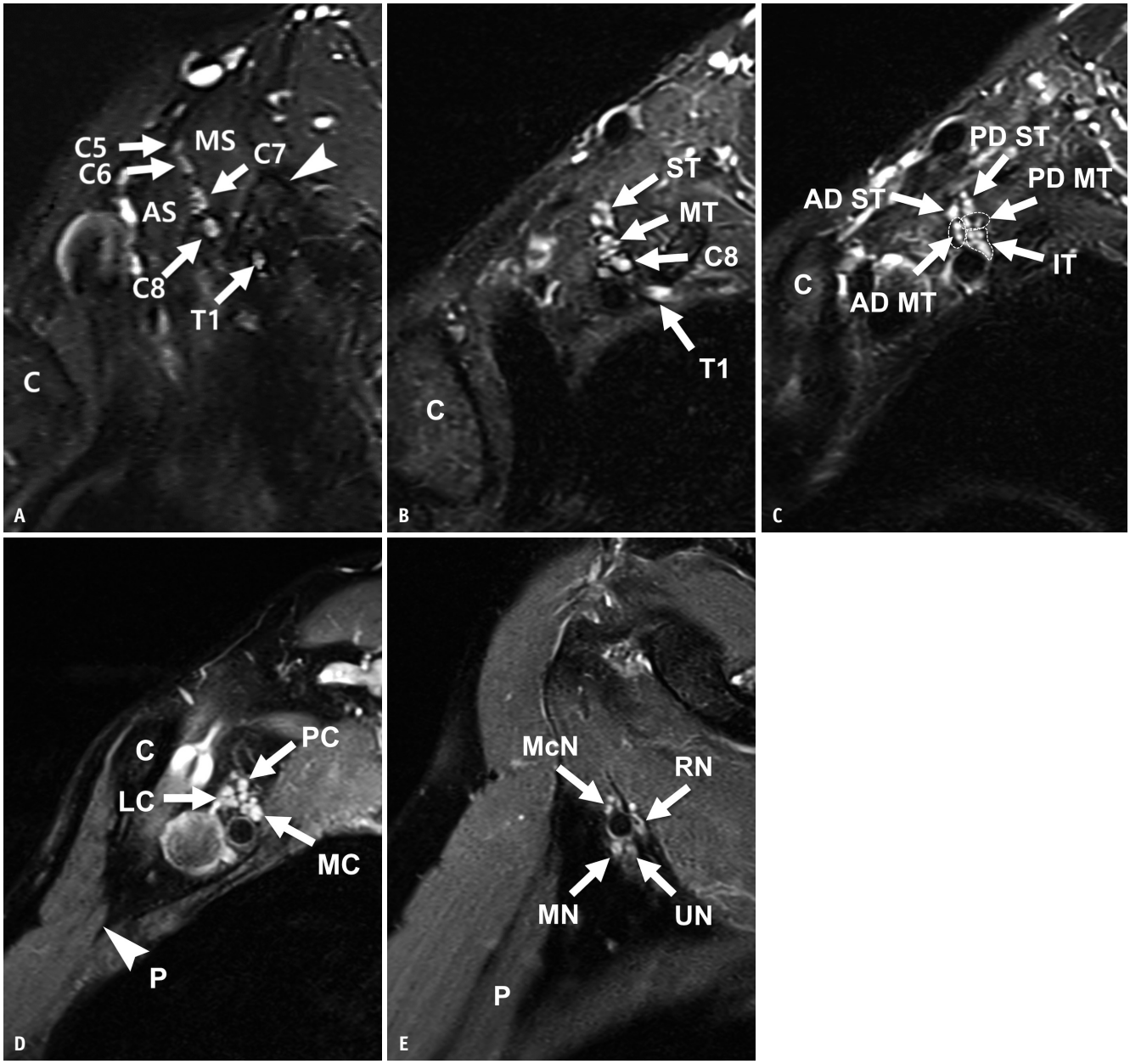

Fig. 7. Normal anatomy: brachial plexus. Oblique sagittal fat-suppressed T2-weighted images from medial to lateral direction. The anterior scalene (AS), middle scalene (MS), clavicle (C), and pectoralis minor (P) are the anatomical landmarks used to identify the components of the brachial plexus. **A:** C5-T1 roots (labeled arrows) of the brachial plexus were vertically aligned in the interscalene triangle. The T1 root runs under the first rib (arrowhead) and approaches the C8 root to form an inferior trunk (IT). **B:** The superior trunk (ST) and middle trunk (MT) (labeled arrows) were located at the lateral border of the interscalene triangle. The C8 and T1 roots (labeled arrows) combined in a more lateral position to form the IT. **C:** In the retroclavicular area, the anterior division (AD) and posterior divisions (PD) of the trunks (labeled arrows) are identifiable. Dashed lines indicate the boundary of the divisions of MT and IT. **D:** At the infraclavicular level, posterior cord (PC), lateral cord (LC), and medial cord (MC) (labeled arrows) are arranged in a triangular form. Labeled arrowhead indicates pectoralis minor. **E:** The brachial plexus terminal branches (RN, radial nerve; UN, ulnar nerve; MN, median nerve; McN, musculocutaneous nerve) (labeled arrows) are arranged in a circle around the subclavian artery.

contrast, type B designates nerve divisions occurring between and beneath the two muscle heads (11.7%). Type C entails divisions above and below the undivided muscles (3.3%). Type D involves an unpartitioned nerve situated amidst the two muscle heads. Type E corresponds to divisions occurring between and above the two muscle heads. Lastly, type F designates an unpartitioned nerve positioned above the undivided muscle. Notably, types D, E,

https://doi.org/10.3348/kjr.2023.0150

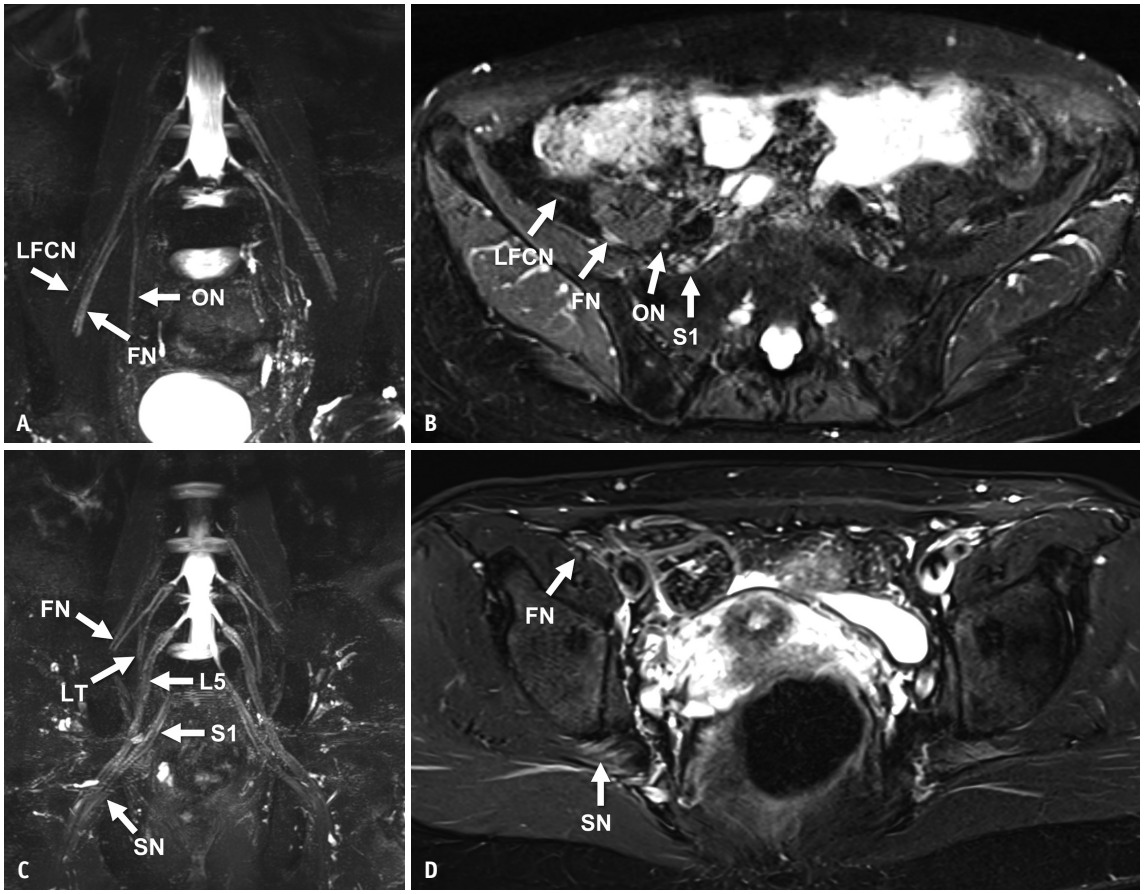

Fig. 8. Normal anatomy: lumbosacral plexus. Coronal three-dimensional (3D) short-tau inversion recovery fast spin-echo (STIR-FSE) with a 10 mm slab and maximal intensity projection, along with axial two-dimensional (2D) fat-suppressed, T2-weighted FSE images captured following intravenous gadolinium contrast agent administration, reveal specific anatomical features. **A, B:** The femoral nerve (FN) and lateral femoral cutaneous nerve (LFCN) (labeled arrows) exhibit a parallel trajectory anterior to the psoas muscle, with the FN coursing through the groove between the psoas and iliacus muscles in the pelvic cavity. The obturator nerve (ON) (labeled arrows) descends vertically posteromedial to the psoas muscle, while the first sacral nerve (S1) (labeled arrow) is positioned anterior to the sacral ala. **C, D:** The L5 and S1 nerves (labeled arrows) contribute to formation of the sciatic nerve (SN) (labeled arrows). The lumbosacral trunk (LT) (labeled arrow) connects the lumbar and sacral segments of the plexus. The FN (labeled arrows) descends anteriorly towards the femoral canal, passing anterior to the iliopsoas muscle, and the SN emerges posteriorly through the sciatic foramen.

and F are exceedingly rare, each accounting for less than 1% of cases [56].

The trajectory of the sciatic nerve takes it through the subgluteal space, a region encompassed by the gluteal aponeuroses. This space spans from the upper border of the piriformis muscle to the lower margin of the gluteus maximus muscle [57]. Within this context, deep gluteal syndrome (DGS) manifests as an entrapment neuropathy occurring within the subgluteal space, encompassing conditions such as piriformis syndrome [57,58]. Other contributors to DGS encompass obturator internus/gemellus syndrome, ischiofemoral impingement, hamstring tendinopathy, and various gluteal disorders.

A recent notable advancement is the identification and endoscopic release of a fibrovascular band, which can either compress or adhere to the sciatic nerve. This approach has changed the diagnostic and therapeutic paradigms associated with piriformis syndrome [59]. The pudendal nerve (ventral rami of S2, S3-S4) is sensory to the external genitalia and perineum and motor to the perineum and pelvic floor muscles and exits the greater sciatic foramen between the piriformis and coccygeus muscles. After crossing the ischial spine, the pudendal nerve reenters the pelvis through the lesser sciatic foramen, between the sacrospinous and sacrotuberous ligaments. The pudendal canal, also known as Alcock's canal, houses the pudendal nerve. Most pudendal nerve entrapments occur in Alcock's canal or between the sacrotuberous and sacrospinous ligaments. Importantly, the MRN guides perineural injections by identifying compressive masses, perineural scarring, or

https://doi.org/10.3348/kjr.2023.0150

Korean Journal of Radiology
KJR

nerve signal change [60]. Furthermore, comparison with the contralateral nerve can help identify subtle signal changes in the pudendal nerve [61].

Interpretation of MRN

On T2-weighted images, the signal intensity of normal peripheral nerves is slightly higher than that of adjacent skeletal muscles because the T2-relaxation times of skeletal muscle and peripheral nerves on 3T MRI are approximately 50 ms and 80 ms, respectively [29]. Increased signal intensity of the peripheral nerve is the most frequent feature of peripheral neuropathy on MRN and is usually evident within 24 hours following an insult [62]. The signal alteration is maximal adjacent to the area of entrapment or injury, which helps localize the site of the insult [63]. However, a signal increase can occur in normal nerves as a magic-angle phenomenon on intermediate-weighted sequences or as a normal variation in the elbow or wrist [64,65]. Generally, a nerve signal approaching a fluid signal is considered abnormal. Thus, a comparison with the unaffected contralateral nerve may be useful because the intensity and length of signal alterations are more pronounced in the injured nerve than in the contralateral nerves [63,66]. The increased signal intensity of peripheral nerves should be interpreted in conjunction with architectural distortion, deviation of course, caliber changes, and perineural fibrosis.

The internal fascicular architecture has a striated appearance on longitudinal images and a honeycomb pattern on axial images of large nerves [67]. Importantly, individual fascicles must maintain their signal, caliber, and continuity. The normal peripheral nerve follows a smooth and continuous path, gradually tapering its caliber along its length, and deviations from the expected course, irregular contours, and abrupt nerve caliber changes indicate entrapment neuropathy. A high-grade injury is indicated by focal bulging with nerve continuity on either side, representing the NIC (Fig. 9), or discontinuity of the nerve with an end-bulb neuroma [68]. Peripheral nerves and fascicles are surrounded by perineural and intraneural fat. Obliteration of the fat planes is a sign of perineural fibrosis, which can manifest as late posttraumatic or postoperative sequelae or radiation-induced plexopathy. Apart from the regional fibrotic scar, preganglionic injury can result in a dural diverticula or pseudomeningocele [63,69].

Hourglass constriction (HC) of the nerves is characterized by a focal decrease in caliber unrelated to external compression or entrapment (Fig. 3). MRN frequently reveals HCs rather than plexus-involving lesions in patients with neuralgic amyotrophy with single or combined mononeuropathy patterns [13]. In addition, HCs involving the proximal median or radial nerve fascicles can be associated with anterior or posterior interosseous nerve syndrome [69,70]. Although it is unclear whether HCs

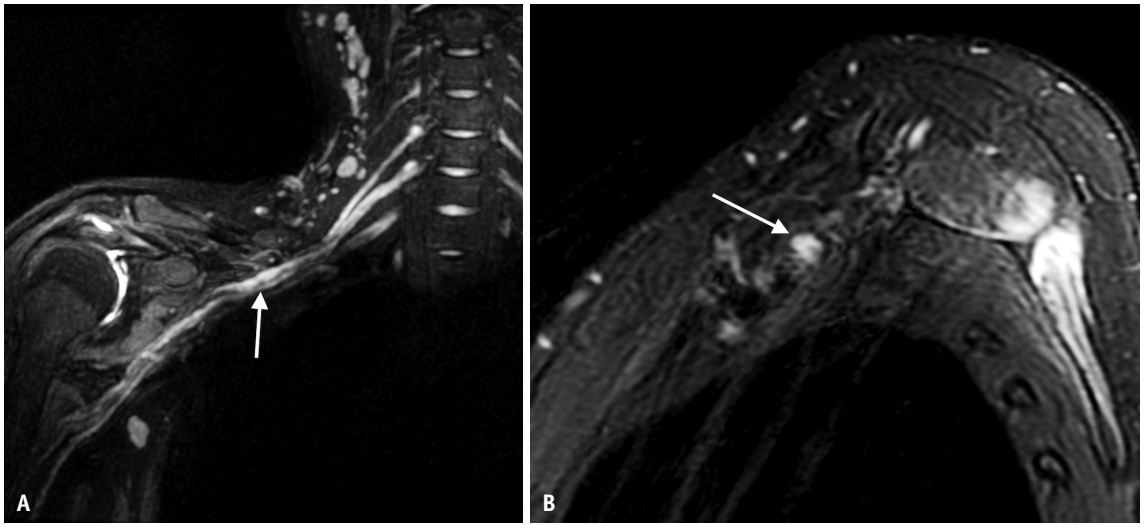

Fig. 9. Pathology: high-grade brachial plexus injury with neuroma-in-continuity. A 23-year-old male with motor weakness in the right shoulder was diagnosed with a preceded by motor vehicle injury. **A:** Coronal maximal intensity projection image of T2-weighted short tau inversion recovery (STIR) with improved motion-sensitized driven-equilibrium (iMSDE) showing that the right posterior cord is focally swollen while maintaining continuity with the adjacent nerve bundles (arrow). **B:** Sagittal chemical shift-encoded water-fat (Dixon method) water image showing focal nodular swelling and increased signal intensity in the posterior cord (arrow). These findings were surgically confirmed to indicate neuroma in continuity.

https://doi.org/10.3348/kjr.2023.0150

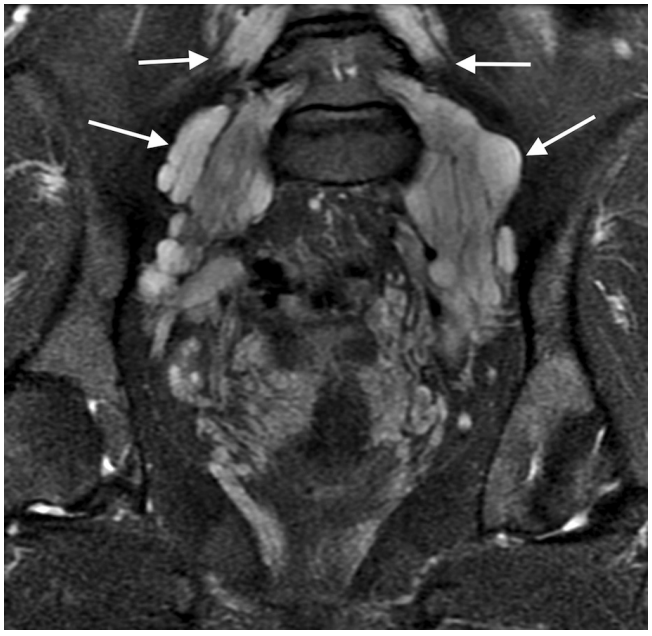

Fig. 10. Pathology: Charcot Marie Tooth (CMT) disease. A 27-year-old female presented with bilateral leg weakness and pes cavity. Coronal fat-suppressed T2-weighted image shows a marked diffuse enlargement of bilateral lumbosacral plexus nerves (arrows) likened to an "onion-bulb" appearance and characteristic of a hereditary neuropathy such as CMT.

are an independent subset of neuropathy or a result of an inflammatory cascade, MRN plays an important role in localizing HCs and assisting in proper management.

The onion-bulb appearance of the nerve represents hypertrophied nerve fascicles caused by repeated demyelination and remyelination [49]. Cross-sectional views show hypertrophic nerves with thickened fascicles containing preserved or effaced intraepineural fat (Fig. 10) [71,72]. These findings are observed in chronic inflammatory demyelinating polyneuropathy and demyelinating subtype of CMT [73]. Moreover, sharp borders of nerve enlargement favor hereditary neuropathy.

CONCLUSION

MRN is technically geared towards achieving a more uniform suppression of background fat and accompanying vessels while preserving the SNR of nerves for imaging of the plexus. With technical advancements, MRN is gaining a substantial impact on diagnostic reasoning and therapeutic treatment recommendations.

Owing to the nonconventional imaging planes and complex paths of nerves, MRN interpretation can be challenging. A clear understanding of plexus anatomy and the spectrum of abnormal findings will facilitate MRN interpretation. The next step would be the transition of quantitative imaging from research to clinical practice.

Conflicts of Interest

The authors have no potential conflicts of interest to disclose.

Author Contributions

Conceptualization: John A Carrino. Investigation: all authors. Project administration: John A Carrino. Resources: all authors. Supervision: John A Carrino. Visualization: all authors. Writing—original draft: John A Carrino, Joon-Yong Jung. Writing—review & editing: all authors.

ORCID IDs

Joon-Yong Jung
https://orcid.org/0000-0002-6909-0919
Yenpo Lin
https://orcid.org/0000-0001-9617-503X
John A Carrino
https://orcid.org/0000-0003-3472-2469

Funding Statement

None

REFERENCES

1. Filler AG, Howe FA, Hayes CE, Kliot M, Winn HR, Bell BA, et al. Magnetic resonance neurography. *Lancet* 1993;341:659-661
2. Howe FA, Filler AG, Bell BA, Griffiths JR. Magnetic resonance neurography. *Magn Reson Med* 1992;28:328-338
3. Ferrante MA, Wilbourn AJ. Electrodiagnostic approach to the patient with suspected brachial plexopathy. *Neurol Clin* 2002;20:423-450
4. Laughlin RS, Dyck PJ. Electrodiagnostic testing in lumbosacral plexopathies. *Phys Med Rehabil Clin N Am* 2013;24:93-105
5. Chhabra A, Belzberg AJ, Rosson GD, Thawait GK, Chalian M, Farahani SJ, et al. Impact of high resolution 3 tesla MR neurography (MRN) on diagnostic thinking and therapeutic patient management. *Eur Radiol* 2016;26:1235-1244
6. Khodarahmi I, Fritz J. The value of 3 tesla field strength for musculoskeletal magnetic resonance imaging. *Invest Radiol* 2021;56:749-763
7. Ahlawat S, Stern SE, Belzberg AJ, Fritz J. High-resolution metal artifact reduction MR imaging of the lumbosacral plexus in patients with metallic implants. *Skeletal Radiol* 2017;46:897-908
8. Chhabra A, Flammang A, Padua A Jr, Carrino JA, Andreisek G. Magnetic resonance neurography: technical considerations.

https://doi.org/10.3348/kjr.2023.0150

Neuroimaging Clin N Am 2014;24:67-78
9. Sneag DB, Queler S. Technological advancements in magnetic resonance neurography. *Curr Neurol Neurosci Rep* 2019;19:75
10. Davidson EJ, Tan ET, Pedrick EG, Sneag DB. Brachial plexus magnetic resonance neurography: technical challenges and solutions. *Invest Radiol* 2023;58:14-27
11. Sneag DB, Mendapara P, Zhu JC, Lee SC, Lin B, Curlin J, et al. Prospective respiratory triggering improves high-resolution brachial plexus MRI quality. *J Magn Reson Imaging* 2019;49:1723-1729
12. Del Grande F, Santini F, Herzka DA, Aro MR, Dean CW, Gold GE, et al. Fat-suppression techniques for 3-T MR imaging of the musculoskeletal system. *Radiographics* 2014;34:217-233
13. Sneag DB, Rancy SK, Wolfe SW, Lee SC, Kalia V, Lee SK, et al. Brachial plexitis or neuritis? MRI features of lesion distribution in Parsonage-Turner syndrome. *Muscle Nerve* 2018;58:359-366
14. Khalilzadeh O, Fayad LM, Ahlawat S. 3D MR neurography. *Semin Musculoskelet Radiol* 2021;25:409-417
15. Chhabra A, Subhawong TK, Bizzell C, Flammang A, Soldatos T. 3T MR neurography using three-dimensional diffusion-weighted PSIF: technical issues and advantages. *Skeletal Radiol* 2011;40:1355-1360
16. Chavhan GB, Babyn PS, Jankharia BG, Cheng HL, Shroff MM. Steady-state MR imaging sequences: physics, classification, and clinical applications. *Radiographics* 2008;28:1147-1160
17. Chhabra A, Soldatos T, Subhawong TK, Machado AJ, Thawait SK, Wang KC, et al. The application of three-dimensional diffusion-weighted PSIF technique in peripheral nerve imaging of the distal extremities. *J Magn Reson Imaging* 2011;34:962-967
18. Fujii H, Fujita A, Kanazawa H, Sung E, Sakai O, Sugimoto H. Localization of parotid gland tumors in relation to the intraparotid facial nerve on 3D double-echo steady-state with water excitation sequence. *AJNR Am J Neuroradiol* 2019;40:1037-1042
19. Yoneyama M, Takahara T, Kwee TC, Nakamura M, Tabuchi T. Rapid high resolution MR neurography with a diffusion-weighted pre-pulse. *Magn Reson Med Sci* 2013;12:111-119
20. Kasper JM, Wadhwa V, Scott KM, Rozen S, Xi Y, Chhabra A. SHINKEI--a novel 3D isotropic MR neurography technique: technical advantages over 3DIRTSE-based imaging. *Eur Radiol* 2015;25:1672-1677
21. Wang J, Yarnykh VL, Hatsukami T, Chu B, Balu N, Yuan C. Improved suppression of plaque-mimicking artifacts in black-blood carotid atherosclerosis imaging using a multislice motion-sensitized driven-equilibrium (MSDE) turbo spin-echo (TSE) sequence. *Magn Reson Med* 2007;58:973-981
22. Wang J, Yarnykh VL, Yuan C. Enhanced image quality in black-blood MRI using the improved motion-sensitized driven-equilibrium (iMSDE) sequence. *J Magn Reson Imaging* 2010;31:1256-1263
23. Chen WC, Tsai YH, Weng HH, Wang SC, Liu HL, Peng SL, et al. Value of enhancement technique in 3D-T2-STIR images of the brachial plexus. *J Comput Assist Tomogr* 2014;38:335-339
24. Zhang Y, Kong X, Zhao Q, Liu X, Gu Y, Xu L. Enhanced MR neurography of the lumbosacral plexus with robust vascular suppression and improved delineation of its small branches. *Eur J Radiol* 2020;129:109128
25. Sneag DB, Daniels SP, Geannette C, Queler SC, Lin BQ, de Silva C, et al. Post-contrast 3D inversion recovery magnetic resonance neurography for evaluation of branch nerves of the brachial plexus. *Eur J Radiol* 2020;132:109304
26. Daldrup-Link HE. Ten things you might not know about iron oxide nanoparticles. *Radiology* 2017;284:616-629
27. Queler SC, Tan ET, Geannette C, Prince M, Sneag DB. Ferumoxytol-enhanced vascular suppression in magnetic resonance neurography. *Skeletal Radiol* 2021;50:2255-2266
28. Sneag DB, Zochowski KC, Tan ET. MR neurography of peripheral nerve injury in the presence of orthopedic hardware: technical considerations. *Radiology* 2021;300:246-259
29. Stanisz GJ, Odrobina EE, Pun J, Escaravage M, Graham SJ, Bronskill MJ, et al. T1, T2 relaxation and magnetization transfer in tissue at 3T. *Magn Reson Med* 2005;54:507-512
30. Takahara T, Imai Y, Yamashita T, Yasuda S, Nasu S, Van Cauteren M. Diffusion weighted whole body imaging with background body signal suppression (DWIBS): technical improvement using free breathing, STIR and high resolution 3D display. *Radiat Med* 2004;22:275-282
31. Yamashita T, Kwee TC, Takahara T. Whole-body magnetic resonance neurography. *N Engl J Med* 2009;361:538-539
32. Jambawalikar S, Baum J, Button T, Li H, Geronimo V, Gould ES. Diffusion tensor imaging of peripheral nerves. *Skeletal Radiol* 2010;39:1073-1079
33. Jeon T, Fung MM, Koch KM, Tan ET, Sneag DB. Peripheral nerve diffusion tensor imaging: overview, pitfalls, and future directions. *J Magn Reson Imaging* 2018;47:1171-1189
34. Cauley KA, Filippi CG. Diffusion-tensor imaging of small nerve bundles: cranial nerves, peripheral nerves, distal spinal cord, and lumbar nerve roots--clinical applications. *AJR Am J Roentgenol* 2013;201:W326-W335
35. Bäumer P, Pham M, Ruetters M, Heiland S, Heckel A, Radbruch A, et al. Peripheral neuropathy: detection with diffusion-tensor imaging. *Radiology* 2014;273:185-193
36. Yamasaki T, Fujiwara H, Oda R, Mikami Y, Ikeda T, Nagae M, et al. In vivo evaluation of rabbit sciatic nerve regeneration with diffusion tensor imaging (DTI): correlations with histology and behavior. *Magn Reson Imaging* 2015;33:95-101
37. Farinas AF, Pollins AC, Stephanides M, O'Neill D, Al-Kassis S, Esteve IVM, et al. Diffusion tensor tractography to visualize axonal outgrowth and regeneration in a 4-cm reverse autograft sciatic nerve rabbit injury model. *Neurol Res* 2019;41:257-264
38. Fritz J, Ahlawat S. Getting quantitative diffusion-weighted MR neurography and tractography ready for clinical practice. *J Magn Reson Imaging* 2020;51:1138-1139
39. Foesleitner O, Sulaj A, Sturm V, Kronlage M, Godel T, Preisner F, et al. Diffusion MRI in peripheral nerves: optimized b values and the role of non-gaussian diffusion. *Radiology* 2022;302:153-161

 https://doi.org/10.3348/kjr.2023.0150

40. Martín-Noguerol T, Montesinos P, Barousse R, Luna A. RadioGraphics update: functional MR neurography in evaluation of peripheral nerve trauma and postsurgical assessment. *Radiographics* 2021;41:E40-E44
41. Sneag DB, Zochowski KC, Tan ET, Queler SC, Burge A, Endo Y, et al. Denoising of diffusion MRI improves peripheral nerve conspicuity and reproducibility. *J Magn Reson Imaging* 2020;51:1128-1137
42. Zochowski KC, Tan ET, Argentieri EC, Lin B, Burge AJ, Queler SC, et al. Improvement of peripheral nerve visualization using a deep learning-based MR reconstruction algorithm. *Magn Reson Imaging* 2022;85:186-192
43. Antun V, Renna F, Poon C, Adcock B, Hansen AC. On instabilities of deep learning in image reconstruction and the potential costs of AI. *Proc Natl Acad Sci U S A* 2020;117:30088-30095
44. Antoniadis G. *The peripheral nerve: neuroanatomical principles before and after injury*. In: Haastert-Talini K, Assmus H, Antoniadis G, eds. *Modern concepts of peripheral nerve repair*. 1st ed. Cham: Springer, 2017:1-10
45. Weerasuriya A, Mizisin AP. The blood-nerve barrier: structure and functional significance. *Methods Mol Biol* 2011;686:149-173
46. Kubiak CA, Kung TA, Brown DL, Cederna PS, Kemp SWP. State-of-the-art techniques in treating peripheral nerve injury. *Plast Reconstr Surg* 2018;141:702-710
47. Cattin AL, Lloyd AC. The multicellular complexity of peripheral nerve regeneration. *Curr Opin Neurobiol* 2016;39:38-46
48. Seddon HJ, Medawar PB, Smith H. Rate of regeneration of peripheral nerves in man. *J Physiol* 1943;102:191-215
49. Chung T, Prasad K, Lloyd TE. Peripheral neuropathy: clinical and electrophysiological considerations. *Neuroimaging Clin N Am* 2014;24:49-65
50. Sunderland S. A classification of peripheral nerve injuries producing loss of function. *Brain* 1951;74:491-516
51. Mackinnon SE. Dellon AL. *Surgery of the peripheral nerve*. 1st ed. New York: Thieme Medical Publishers, 1988:74-78
52. Thawait SK, Wang K, Subhawong TK, Williams EH, Hashemi SS, Machado AJ, et al. Peripheral nerve surgery: the role of high-resolution MR neurography. *AJNR Am J Neuroradiol* 2012;33:203-210
53. Gilcrease-Garcia BM, Deshmukh SD, Parsons MS. Anatomy, imaging, and pathologic conditions of the brachial plexus. *Radiographics* 2020;40:1686-1714
54. Leonhard V, Smith R, Caldwell G, Smith HF. Anatomical variations in the brachial plexus roots: implications for diagnosis of neurogenic thoracic outlet syndrome. *Ann Anat* 2016;206:21-26
55. Beaton LE, Anson BJ. The relation of the sciatic nerve and of its subdivisions to the piriformis muscle. *Anat Rec* 1937;70:1-5
56. Eastlack J, Tenorio L, Wadhwa V, Scott K, Starr A, Chhabra A. Sciatic neuromuscular variants on MR neurography: frequency study and interobserver performance. *Br J Radiol* 2017;90:20170116
57. Hernando MF, Cerezal L, Pérez-Carro L, Abascal F, Canga A. Deep gluteal syndrome: anatomy, imaging, and management of sciatic nerve entrapments in the subgluteal space. *Skeletal Radiol* 2015;44:919-934
58. Koh E. Imaging of peripheral nerve causes of chronic buttock pain and sciatica. *Clin Radiol* 2021;76:626.e1-626.e11
59. Martin HD, Shears SA, Johnson JC, Smathers AM, Palmer IJ. The endoscopic treatment of sciatic nerve entrapment/deep gluteal syndrome. *Arthroscopy* 2011;27:172-181
60. Ly J, Scott K, Xi Y, Ashikyan O, Chhabra A. Role of 3 tesla MR neurography and CT-guided injections for pudendal neuralgia: analysis of pain response. *Pain Physician* 2019;22:E333-E344
61. Lo L, Duarte A, Bencardino JT. Nerve entrapments in the pelvis and hip. *Semin Musculoskelet Radiol* 2022;26:153-162
62. Bendszus M, Wessig C, Solymosi L, Reiners K, Koltzenburg M. MRI of peripheral nerve degeneration and regeneration: correlation with electrophysiology and histology. *Exp Neurol* 2004;188:171-177
63. Chalian M, Chhabra A. Top-10 tips for getting started with magnetic resonance neurography. *Semin Musculoskelet Radiol* 2019;23:347-360
64. Soldatos T, Andreisek G, Thawait GK, Guggenberger R, Williams EH, Carrino JA, et al. High-resolution 3-T MR neurography of the lumbosacral plexus. *Radiographics* 2013;33:967-987
65. Miller TT, Reinus WR. Nerve entrapment syndromes of the elbow, forearm, and wrist. *AJR Am J Roentgenol* 2010;195:585-594
66. Kim S, Chung BM, Kim WT, Lee GY, Hur J, Kim JH, et al. Diagnosing ulnar neuropathy at the elbow on MRI: importance of the longitudinal extent of the hyperintense ulnar nerve. *Skeletal Radiol* 2022;51:1473-1481
67. Chhabra A, Madhuranthakam AJ, Andreisek G. Magnetic resonance neurography: current perspectives and literature review. *Eur Radiol* 2018;28:698-707
68. Chhabra A, Williams EH, Wang KC, Dellon AL, Carrino JA. MR neurography of neuromas related to nerve injury and entrapment with surgical correlation. *AJNR Am J Neuroradiol* 2010;31:1363-1368
69. Yasunaga H, Shiroishi T, Ohta K, Matsunaga H, Ota Y. Fascicular torsion in the median nerve within the distal third of the upper arm: three cases of nontraumatic anterior interosseous nerve palsy. *J Hand Surg Am* 2003;28:206-211
70. Rossey-Marec D, Simonet J, Beccari R, Michot C, Bencteux P, Dacher JN, et al. Ultrasonographic appearance of idiopathic radial nerve constriction proximal to the elbow. *J Ultrasound Med* 2004;23:1003-1007
71. Thawait SK, Chaudhry V, Thawait GK, Wang KC, Belzberg A, Carrino JA, et al. High-resolution MR neurography of diffuse peripheral nerve lesions. *AJNR Am J Neuroradiol* 2011;32:1365-1372
72. Kronlage M, Bäumer P, Pitarokoili K, Schwarz D, Schwehr V, Godel T, et al. Large coverage MR neurography in CIDP: diagnostic accuracy and electrophysiological correlation. *J Neurol* 2017;264:1434-1443
73. Oka N, Kawasaki T, Unuma T, Shigematsu K, Sugiyama H. Different profiles of onion bulb in CIDP and CMT1A in relation to extracellular matrix. *Clin Neuropathol* 2013;32:406-412

https://doi.org/10.3348/kjr.2023.0150